Tellus (1994), 46A, 178–199
Printed in Belgium – all rights reserved

TELLUS
ISSN 0280–6495

Modeling tides in the western North Atlantic using unstructured graded grids

By J. J. WESTERINK[1]*, R. A. LUETTICH, JR.[2] and J. C. MUCCINO[1], [1]*Department of Civil Engineering and Geological Sciences, University of Notre Dame, Notre Dame, IN 46556 USA*; [2]*University of North Carolina at Chapel Hill, Institute of Marine Sciences, 3431 Arendell Street, Morehead City, NC 28557 USA*

(Manuscript received 1 December 1992; in final form 1 July 1993)

ABSTRACT

This paper describes grid convergence studies for a finite-element-based tidal model of the western North Atlantic, Gulf of Mexico and Caribbean. The very large computational domain used for this tidal model encompasses both the coastal and the deep ocean and facilitates the specification of boundary conditions. Due to the large variability in depths as well as scale content of the tides within the model domain, an optimal unstructured graded grid with highly variable finite element areas is developed which significantly reduces the size of the discrete problem while improving the accuracy of the computations. The convergence studies include computations for a sequence of regularly discretized grids ranging from a very coarse $1.6° \times 1.6°$ mesh to a very fine $6' \times 6'$ to $12' \times 12'$ mesh as well as unstructured graded grids with resolutions varying between $1.6°$ and $5'$ within each mesh. Resolution requirements are related to depth, gradients in topography as well as the resolution of the coastal boundary. The final optimal graded grid has a tidal response which is comparable to that of the finest regular grid in most regions. The optimal graded grid is then forced with Schwiderski's (1979, 1980, 1981a–g) global model on the open ocean boundary and tidal potential forcing functions within the interior domain. The structure of the tides is examined, computed co-tidal charts are presented and comparisons are made between the computed results and field data at 77 stations within the model domain.

1. Introduction

There has been a recent trend in coastal ocean tidal modeling towards using increasingly larger computational domains which extend up to or beyond the continental shelf break and slope. For example Flather (1987), Gerritsen and Bijlsma (1988), and Vincent and Le Provost (1988) have all developed tidal and/or storm surge models of a large portion of the eastern North Atlantic. These studies indicate that accurate tidal predictions can be conveniently obtained using large computational domains. In this paper, we present initial results from a tidal model of the western North Atlantic which incompasses the coastal ocean as well as the deep ocean. Key features of our Western North Atlantic Tidal (WNAT) model are the definition of hydrodynamically simple open ocean boundaries to facilitate the specification of boundary conditions, the use of a high degree of selective grid refinement to resolve the flow physics on a localized basis and the coupling of the coastal ocean with a global tidal model.

The domain for the WNAT model encompasses the Western North Atlantic ocean, the Caribbean Sea and the Gulf of Mexico. The WNAT model has an eastern open ocean boundary which lies along the 60° W meridian and is situated almost entirely in the deep ocean. The location of this open ocean boundary was specifically selected

* Corresponding author.

to simplify the difficult task of specifying an accurate set of boundary conditions for a coastal ocean tidal model. The WNAT model open ocean boundary offers a variety of significant advantages. First, the boundary is geometrically simple and includes no discontinuities or corners. Second, the boundary lies almost entirely in the deep ocean where tides vary gradually. This avoids the difficulty of specifying complex and highly variable cross shelf boundary conditions over most of the open ocean boundary. Furthermore this open ocean boundary is ideally suited for coupling with global tidal models which should be most accurate in the deep ocean. Third, nonlinear tidal constituents will not be significant on this open boundary since they are generated on the continental shelf and are largely trapped on the shelf due to the out of phase reflective character of the continental slope.

The size of the resulting computational domain of the WNAT model exceeds 8×10^6 km^2 and is therefore very large in terms of coastal ocean tidal models. It is clear that to uniformly discretize the entire domain with the resolution required in regions of rapidly varying flow, would substantially increase the size of the discrete problem. In fact, in deep ocean regions, which account for more than three quarters of the domain, a relatively coarse discretization should resolve all flow features of interest. However, on the continental shelf, the propagation speed and wavelength of tidal waves decrease with decreasing bathymetric depth and therefore require an increasingly finer discretization. Flow also varies much more quickly in regions of rapidly varying topography, such as in the vicinity of the continental shelf break and the continental slope, as well as near the coastal boundary. Therefore, these regions should require a greater resolution than deep ocean regions.

In order to realize tidal computations on highly unstructured graded grids, we have implemented a Generalized Wave Continuity Equation (GWCE) based finite element (FE) shallow water model (Lynch and Gray, 1979; Kinnmark, 1984; Luettich et al., 1992). GWCE based FE solutions to the shallow water equations have been demonstrated to lead to highly accurate and robust hydrodynamic circulation predictions within the coastal and deep oceans (Lynch, 1983; Le Provost and Vincent, 1986; Foreman, 1988; Vincent and Le Provost, 1988; Walters, 1988; Gray, 1989; Walters and Werner, 1989; Werner and Lynch, 1989; Westerink et al., 1992a).

In this paper, we systematically examine resolution requirements for the WNAT model using the entire model domain. It is vital to establish the level of convergence achieved with the grid resolution used in a computational domain (Le Provost and Vincent, 1986; Dietrich et al., 1990). We present computations for a sequence of regularly discretized grids ranging from a very coarse $1.6^\circ \times 1.6^\circ$ mesh to a very fine $6' \times 6'$ to $12' \times 12'$ mesh. These are compared to a sequence of unstructured graded grids with resolutions varying between 1.6° and $5'$ within each mesh. In the development of an optimal graded grid, we have carefully considered the resolution requirements in regions of rapidly varying topography as well as the resolution of the coastal boundary. The final optimal graded grid has a tidal response which is comparable to that of the finest regular grid in most regions. We then couple the WNAT model, using our optimal graded grid, with Schwiderski's (1979, 1980, 1981a–g) global model. Computed co-tidal charts are presented for eight astronomical constituents and comparisons are made between the computed results and field data at 77 stations within the WNAT domain.

2. Governing equations and numerical discretization

The computations described in this paper were performed using ADCIRC-2DDI, the depth integrated option of a system of two and three dimensional hydrodynamic codes named ADCIRC (Luettich et al., 1992). ADCIRC-2DDI uses the depth integrated equations of mass and momentum conservation, subject to the incompressibility, Boussinesq and hydrostatic pressure approximations. Using the standard quadratic parameterization for bottom stress and neglecting baroclinic terms and lateral diffusion/dispersion effects leads to the following set of conservation statements in primitive non-conservative form expressed in a spherical coordinate system (Flather, 1988; Kolar et al., 1993):

$$\frac{\partial \zeta}{\partial t} + \frac{1}{R \cos \phi}\left(\frac{\partial UH}{\partial \lambda} + \frac{\partial (VH \cos \phi)}{\partial \phi}\right) = 0, \qquad (1)$$

$$\frac{\partial U}{\partial t}+\frac{1}{R\cos\phi}U\frac{\partial U}{\partial\lambda}+\frac{1}{R}V\frac{\partial U}{\partial\phi}-\left(\frac{\tan\phi}{R}U+f\right)V$$
$$=-\frac{1}{R\cos\phi}\frac{\partial}{\partial\lambda}\left[\frac{p_s}{\rho_0}+g(\zeta-\eta)\right]+\frac{\tau_{s\lambda}}{\rho_0 H}-\tau_* U \quad (2)$$

$$\frac{\partial V}{\partial t}+\frac{1}{R\cos\phi}U\frac{\partial V}{\partial\lambda}+\frac{1}{R}V\frac{\partial V}{\partial\phi}+\left(\frac{\tan\phi}{R}U+f\right)U$$
$$=-\frac{1}{R}\frac{\partial}{\partial\phi}\left[\frac{p_s}{\rho_0}+g(\zeta-\eta)\right]+\frac{\tau_{s\phi}}{\rho_0 H}-\tau_* V, \quad (3)$$

where

t = time
λ, ϕ = degrees longitude (east of Greenwich positive) and degrees lattitude (north of the equator positive)
ζ = free surface elevation relative to the geoid
U, V = depth averaged horizontal velocities
R = radius of the earth
H = $\zeta + h$ = total water column
h = bathymetric depth relative to the geoid
f = $2\Omega \sin\phi$ = Coriolis parameter
Ω = angular speed of the earth
p_s = atmospheric pressure at the free surface
g = acceleration due to gravity
η = effective Newtonian equilibrium tide potential
ρ_0 = reference density of water
τ_{sx}, τ_{sy} = applied free surface stress

$$\tau_* = C_f\frac{(U^2+V^2)^{1/2}}{H}$$

C_f = bottom friction coefficient

A practical expression for the effective Newtonian equilibrium tide potential is given by Reid (1990) as:

$$\eta(\lambda,\phi,t)=\sum_{n,j}\alpha_{jn}C_{jn}f_{jn}(t_0)\,L_j(\phi)$$
$$\times\cos[2\pi(t-t_0)/T_{jn}+j\lambda+v_{jn}(t_0)] \quad (4)$$

where

C_{jn} = constant characterizing the amplitude of tidal constituent n of species j
α_{jn} = effective earth elasticity factor for tidal constituent n of species j
f_{jn} = time dependent nodal factor
v_{jn} = time dependent astronomical argument
$j = 0, 1, 2$ = tidal species ($j=0$, declinational; $j=1$, diurnal; $j=2$, semi-diurnal)
L_0 = $3\sin^2\phi - 1$
L_1 = $\sin(2\phi)$
L_2 = $\cos^2(\phi)$
λ, ϕ = degrees longitude and latitude, respectively
t_0 = reference time
T_{jn} = period of constituent n of species j

Values for C_{jn} are presented by Reid (1990). We note that the value for the effective earth elasticity factor is typically taken as 0.69 for all tidal constituents (Schwiderski, 1980; Hendershott, 1981) although its value has been shown to be slightly constituent dependent (Wahr, 1981; Woodworth, 1990).

To facilitate a FE solution to eqs., (1)–(3), these equations are mapped from spherical form into a rectilinear coordinate system using a Carte Parallelogrammatique (CP) projection (Pearson, 1990):

$$x' = R(\lambda-\lambda_0)\cos\phi_0, \quad (5)$$

$$y' = R\phi, \quad (6)$$

where λ_0, ϕ_0 = center point of the projection. Applying the CP projection to eqs. (1)–(3) gives the shallow water equations in primitive nonconservative form expressed in the CP coordinate system:

$$\frac{\partial\zeta}{\partial t}+\frac{\cos\phi_0}{\cos\phi}\frac{\partial(UH)}{\partial x'}+\frac{1}{\cos\phi}\frac{\partial(VH\cos\phi)}{\partial y'}=0, \quad (7)$$

$$\frac{\partial U}{\partial t}+\frac{\cos\phi_0}{\cos\phi}U\frac{\partial U}{\partial x'}+V\frac{\partial U}{\partial y'}-\left(\frac{\tan\phi}{R}U+f\right)V$$
$$=-\frac{\cos\phi_0}{\cos\phi}\frac{\partial}{\partial x'}\left[\frac{p_s}{\rho_0}+g(\zeta-\eta)\right]$$
$$+\frac{\tau_{s\lambda}}{\rho_0 H}-\tau_* U, \quad (8)$$

$$\frac{\partial V}{\partial t}+\frac{\cos\phi_0}{\cos\phi}U\frac{\partial V}{\partial x'}+V\frac{\partial V}{\partial y'}+\left(\frac{\tan\phi}{R}U+f\right)U$$
$$=-\frac{\partial}{\partial y'}\left[\frac{p_s}{\rho_0}+g(\zeta-\eta)\right]+\frac{\tau_{s\phi}}{\rho_0 H}-\tau_* V. \quad (9)$$

Utilizing the FE method to resolve the spatial dependence in the shallow water equations in their primitive form gives inaccurate solutions with severe artificial near $2 \cdot \Delta x$ modes (Gray, 1982). However, reformulating the primitive equations into a Generalized Wave Continuity Equation (GWCE) form gives highly accurate, noise free, FE based solutions to the shallow water equations (Lynch and Gray, 1979; Kinnmark, 1984). The GWCE is derived by combining a time differentiated form of the primitive continuity equation and a spatially differentiated form of the primitive momentum equations recast into conservative form, reformulating the convective terms into non-conservative form and adding the primitive form of the continuity equation multiplied by a constant in time and space, τ_0 (Lynch and Gray, 1979; Kinnmark, 1984; Luettich et al., 1992). The GWCE in the CP coordinate system is:

$$\frac{\partial^2 \zeta}{\partial t^2} + \tau_0 \frac{\partial \zeta}{\partial t} + \frac{\cos \phi_0}{\cos \phi} \frac{\partial}{\partial x'} \left[U \frac{\partial \zeta}{\partial t} - \frac{\cos \phi_0}{\cos \phi} UH \frac{\partial U}{\partial x'} \right.$$
$$- VH \frac{\partial U}{\partial y'} + \left(\frac{\tan \phi}{R} U + f \right) VH - H \frac{\cos \phi_0}{\cos \phi}$$
$$\left. \times \frac{\partial}{\partial x'} \left(\frac{p_s}{\rho_0} + g(\zeta - \eta) \right) - (\tau_* - \tau_0) UH + \frac{\tau_{s\lambda}}{\rho_0} \right]$$
$$+ \frac{\partial}{\partial y'} \left[V \frac{\partial \zeta}{\partial t} - \frac{\cos \phi_0}{\cos \phi} UH \frac{\partial V}{\partial x'} - VH \frac{\partial V}{\partial y'} \right.$$
$$- \left(\frac{\tan \phi}{R} U + f \right) UH - H$$
$$\left. \times \frac{\partial}{\partial y'} \left(\frac{p_s}{\rho_0} + g(\zeta - \eta) \right) - (\tau_* - \tau_0) VH + \frac{\tau_{s\phi}}{\rho_0} \right]$$
$$- \frac{\partial}{\partial t} \left[\frac{\tan \phi}{R} VH \right] - \tau_0 \left[\frac{\tan \phi}{R} VH \right] = 0. \qquad (10)$$

The GWCE, (10), is solved in conjunction with the primitive momentum equations in non-conservative form, (8) and (9).

The high accuracy of GWCE based FE solutions is a result of their excellent numerical amplitude and phase propagation characteristics. In fact, Fourier analysis indicates that in constant depth water and using linear interpolation, a linear tidal wave resolved with 25 nodes per wavelength is more than adequately resolved over the range of Courant numbers, $C = \sqrt{gh}\, \Delta t / \Delta x \leqslant 1.0$ (Luettich et al., 1992). Furthermore, the monotonic dispersion behavior of GWCE based FE solutions avoids generating artificial near $2 \cdot \Delta x$ modes which plague primitive based FE solutions (Platzman, 1981; Foreman, 1983). We note that the monotonic dispersion behavior of GWCE based FE solutions is very similar to that associated with staggered finite difference solutions to the primitive shallow water equations (Westerink and Gray, 1991). GWCE based FE solutions to the shallow water equations allow for extremely flexible spatial discretizations which result in a highly effective minimization of the discrete size of any problem (Le Provost and Vincent, 1986; Foreman, 1988; Vincent and Le Provost, 1988; Westerink et al., 1992a).

The details of ADCIRC, our implementation of the GWCE based solution to the shallow water equations, are described by Luettich et al. (1992). As most GWCE based FE codes, ADCIRC applies three noded linear triangles for surface elevation, velocity and depth. Furthermore, the decoupling of the time and space discrete form of the GWCE and momentum equations, time independent and/or tri-diagonal system matrices, elimination of spatial integration procedures during time stepping and full vectorization of all major loops results in a highly efficient code.

3. Description of the computational domain

The WNAT model domain is shown in Fig. 1. The open ocean boundary extends from the vicinity of Glace Bay in Nova Scotia, Canada to the vicinity of Corocora Island in eastern Venezuela. The computational domain is bounded on the north, west and south by the North, Central and South American coastlines. The topography within the domain, shown in Fig. 1, includes the continental shelf (depths typically range from 0 m to 130 m), the continental slope (depths typically range from 130 m to 3000 m) and the continental rise and deep ocean (depths from approximately 3000 m to almost 8500 m).

The WNAT model open ocean boundary lies almost entirely in the deep ocean well away from the continental shelf and slope. As was discussed in the introduction, it is highly advantageous to specify boundary conditions in deep water since tides vary slowly, global tidal models tend to be

Tellus A/46/2-6

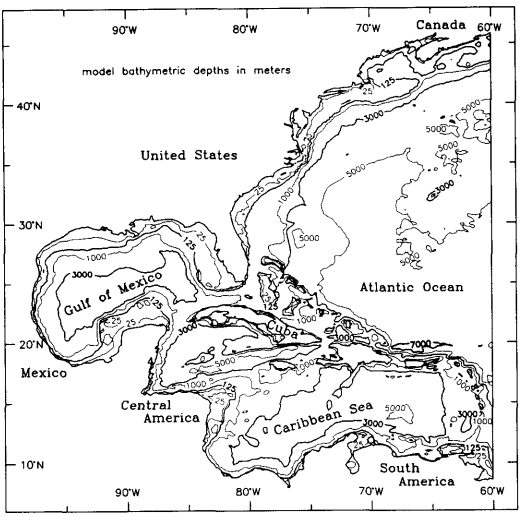

Fig. 1. The Western North Atlantic Tidal (WNAT) model computational domain including bathymetry (m).

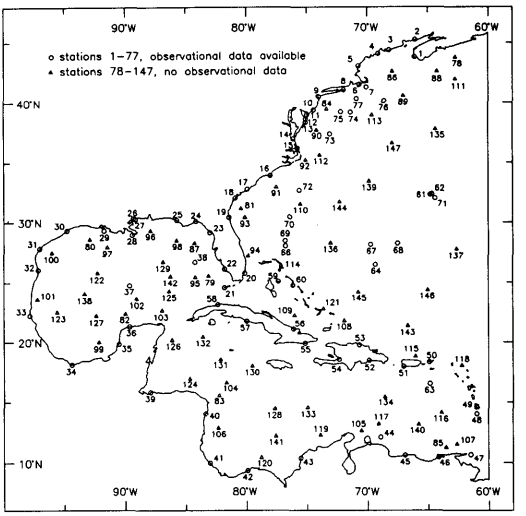

Fig. 2. Locations of tidal elevation stations with available field data and tidal elevation stations without field data within the WNAT computational domain.

more accurate and nonlinear constituents are small in deep water. In water where the model open ocean boundary does cross or come near the continental shelf or slope, there are nearby islands with long term tidal data which allow for adjustments if the global model data proves to be inaccurate in these shallow waters. For example, the very northern portion of the model open ocean boundary crosses the continental shelf and slope but also intersects Sable Island, Canada, which has available tidal data. Furthermore, the southern portion of the open ocean boundary nears or crosses the continental shelf and slope but also is in the vicinity of the lesser Antilles Islands for which long term tidal constituent data exists.

We have defined 147 stations within the WNAT model domain at which tidal elevation time histories were recorded for all model runs. These stations, shown in Fig. 2, provide a basis for inter-grid comparisons and/or comparisons with field measured data.

Stations 1 through 77 have field measured long term tidal elevation data available in harmonically decomposed constituent form (long term indicates that the time history records used to determine the constituent data are typically a year in duration). Data at these stations is obtained from several sources (International Hydrographic Organization Tidal Constituent Bank, 1991; U.S. Geological Survey, 1984; Reid and Whitaker, 1981; and from data bases of the National Ocean Survey, National Oceanographic and Atmospheric Administration, Rockville, MD 20852 USA). These tidal elevation stations lie predominantly in open waters near the coast along the eastern U.S. seaboard (stations 1–20), within the Gulf of Mexico (stations 21–38) and within the Caribbean Sea (stations 39–58). The remaining stations (stations 59–77) are generally located away from the coast either near small islands or in deep waters throughout the WNAT model domain. Stations 1 through 77 were used in the grid convergence studies as well as in comparing the computed tides with the measured field data.

In addition to stations with field measured tidal data, we defined an additional 70 stations throughout the domain in order to achieve a more homogeneous distribution of stations within the domain. The additional stations were placed on the continental shelf (stations 78–87), in the vicinity of the continental shelf break (stations 88–109), near the toe of the continental slope (stations 110–130) and in the deep ocean (stations 131–147). These stations provide a more thorough basis for intercomparisons of responses for the grid convergence studies.

Table 1. *Properties of grids R1 through R5 and V1 through V3*

Grid	Nodes	Boundary	Grid structure	Approximate grid size (°/min)	Approximate grid size (km)	Resolution $\left(\frac{\lambda_{M_2}}{\Delta x}\right)_{max}$	Resolution $\left(\frac{\lambda_{M_2}}{\Delta x}\right)_{min}$	Time step (s)
R1	434	coarse	uniform	1.6°	140	78	1.5	600
R2	1611	coarse	uniform	0.8°	70	162	2.9	300
R3	6191	coarse	uniform	24′	35	341	5.7	150
R4	24255	coarse	uniform	12′	17	704	11.3	75
R5	64065	coarse	semi-uniform	6′ → 12°	8 → 17	1322	22.6	37.5
V1	10147	coarse	graded	5′ → 1.6°	7 → 140	1184	16.0	37.5
V2	27816	coarse	graded	5′ → 1.6°	7 → 140	1013	16.0	37.5
V3	19858	fine	graded	5′ → 1.6°	7 → 140	1344	16.5	37.5

4. Grid convergence studies

In this section, we systematically examine the resolution requirements for the WNAT model for the semi-diurnal astronomical M_2 tide. A sequence of three numerical experiments was conducted to establish the resolution required to obtain a converged M_2 response on a regular grid, to develop an optimal graded grid which minimized the number of nodes within the domain yet gave an M_2 solution that was equivalent to the finest regular grid and to examine the effect of resolution of the boundary on the M_2 solution. The three numerical experiments involved 5 regular grids (R1–R5) and 3 unstructured graded grids (V1–V3). The grid properties are summarized in Table 1. The coarsest and finest regular grids are shown in Figs. 3 and 4 while the three graded meshes are shown in Figs. 5 through 7. All grids were generated using Gredit, a flexible interactive grid generation code developed by Turner and Baptista (1991).

The bathymetry of each grid was obtained by interpolating values from the ETOP05 data base from the National Center for Atmospheric Research which has a resolution of 5′ by 5′. How-

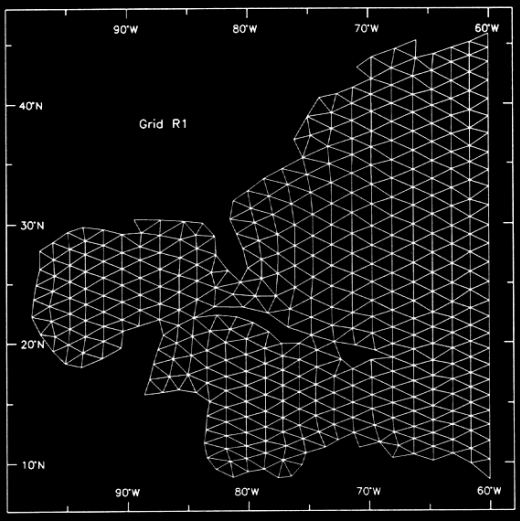

Fig. 3. Grid R1. Regular finite element 1.6° × 1.6° discretization of the domain with a coarse representation of the coastal boundary.

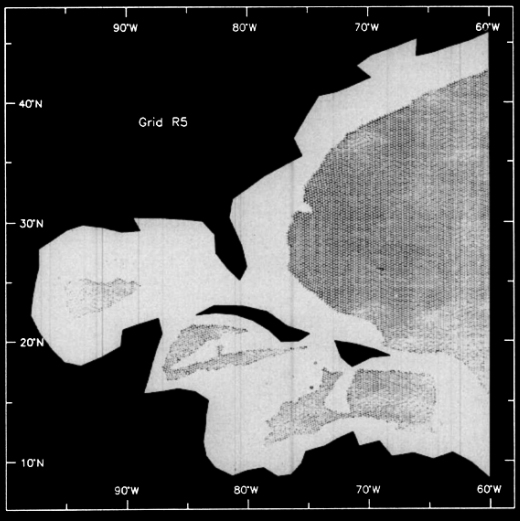

Fig. 4. Grid R5. Nearly regular finite element 6′ × 6′ to 12′ × 12′ discretization of the domain with a coarse representation of the coastal boundary.

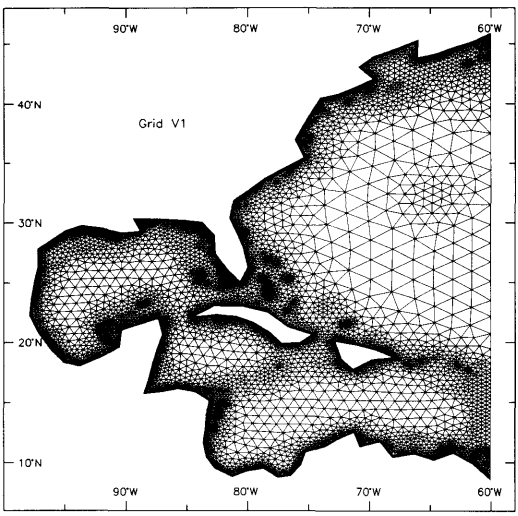

Fig. 5. Grid V1. Unstructured graded finite element discretization of the domain based on a $\lambda_{M_2}/\Delta x \geqslant 25$ criterion with a coarse representation of the coastal boundary.

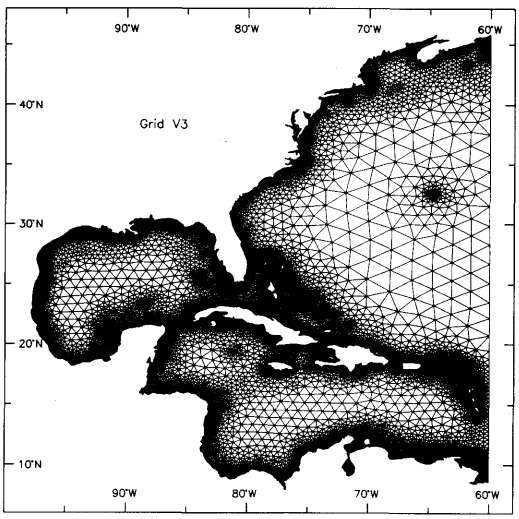

Fig. 7. Grid V3. Unstructured graded finite element discretization of the domain based on a $\lambda_{M_2}/\Delta x \geqslant 25$ criterion with a fine representation of the coastal boundary.

ever, the actual representation of the bathymetry for each grid depends on the grid itself since depth is interpolated linearly on the three noded triangular finite elements. A specified minimum bathymetry of between 4 m (for the Caribbean Sea and Gulf of Mexico) and 7 m (for the northeast US and Canadian coasts) was specified to avoid the drying of elements.

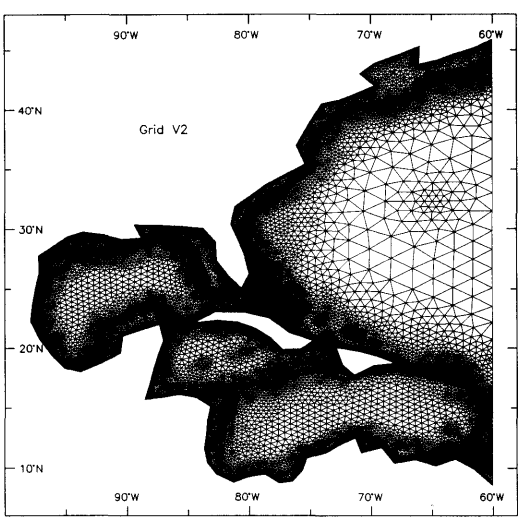

Fig. 6. Grid V2. Unstructured graded finite element discretization of the domain based on a $\lambda_{M_2}/\Delta x \geqslant 25$ criterion with additional resolution in the vicinity of the continental shelf break and with a coarse representation of the coastal boundary.

The open ocean boundary for each grid was forced with an M_2 tidal amplitude and phase interpolated onto the open ocean boundary nodes using data from Schwiderski's (1979) global model results. This results in slightly different boundary forcings in space for grids R1, R2 and R3. Grids R4, R5 and V1 through V3 have essentially identical boundary forcing functions. An effective tidal potential forcing was applied within the domain for the M_2 constituent using an amplitude of 0.242334 meters (Reid, 1990). The theoretical value for the effective Earth elasticity factor (which reduces the magnitude of the tidal potential forcing due to Earth tides) equal to 0.69 was used (Schwiderski, 1980; Hendershott, 1981). Zero normal flow specified boundary conditions were applied to all coastal and island boundaries.

The fully nonlinear form of the shallow water eqs., (1)–(3), was used for all grids. The nonlinear bottom friction coefficient, C_f, was specified equal to 0.003 throughout the domain. The GWCE parameter, τ_0, was specified equal to 0.001 which represents a balance between the primitive continuity and wave equation portions of the GWCE equation.

Time steps used with each grid are listed in Table 1. These time steps were selected to maintain the maximum Courant number based on wave celerity less than unity. Each run was spun up from a cold start applying a very smooth hyperbolic tangent ramp function, which acts over approximately 12 days, to both the boundary and direct forcing functions. The use of this ramp function avoids exciting short period gravity modes and vortex modes in the subinertial frequency range due to start up transients (Reid and Whitaker, 1981). Nonetheless, free Helmholtz modes did appear to be excited in the Gulf of Mexico and the Caribbean Sea. However, the use of the 12 day ramp minimized the amplitude of these modes and they were almost entirely dissipated after about 30 days. Simulations were run for 50 days and tidal elevations were recorded at the 147 defined elevation stations. The last 10 days of these tidal elevation records were analyzed using a least square harmonic analysis and decomposed into amplitudes and phases for the M_2 tide and its overtides.

Comparisons of M_2 elevation amplitudes and phases are the basis for all grid intercomparisons. We present tables of global and regional error measures established by comparing the computed amplitudes and phases to a converged solution (which for our studies was obtained using grid R5). M_2 amplitude errors were computed as a proportional standard deviation for each grid as follows:

$$E^{\text{grid}-\text{R5}}_{M_2-\text{amp}} \equiv \left[\frac{\sum_{l=1}^{L}[\hat{\eta}^{\text{grid}}_{M_2}(x_l, y_l) - \hat{\eta}^{\text{R5}}_{M_2}(x_l, y_l)]^2}{\sum_{l=1}^{L}[\hat{\eta}^{\text{R5}}_{M_2}(x_l, y_l)]^2}\right]^{1/2}, \quad (11)$$

where

L = the total number of elevation stations within a given region,

(x_l, y_l) = the location of an elevation station,

$\hat{\eta}^{\text{grid}}_{M_2}(x_l, y_l)$ = the M_2 elevation amplitude for a given grid at station coordinates (x_l, y_l),

$\hat{\eta}^{\text{R5}}_{M_2}(x_l, y_l)$ = the M_2 elevation amplitude for the converged solution obtained using grid R5 at station coordinates (x_l, y_l).

$E^{\text{grid}-\text{R5}}_{M_2-\text{amp}}$ may be interpreted as the standard deviation in terms of a fraction of a regional representative measure of M_2 amplitude or roughly as an average percentage of error (when multiplied by 100) for the M_2 amplitude within a specified region. M_2 phase errors were computed for each grid as an absolute average error over a defined region as follows:

$$E^{\text{grid}-\text{R5}}_{M_2-\text{phase}} \equiv \frac{1}{L}\sum_{l=1}^{L}|\phi^{\text{grid}}_{M_2}(x_l, y_l) - \phi^{\text{R5}}_{M_2}(x_l, y_l)|, \quad (12)$$

where

$\phi^{\text{grid}}_{M_2}(x_l, y_l)$ = the M_2 elevation phase for a given grid at measurement location (x_l, y_l),

$\phi^{\text{R5}}_{M_2}(x_l, y_l)$ = the M_2 elevation phase for the converged solution obtained with grid R5 at measurement location (x_l, y_l).

$E^{\text{grid}-\text{R5}}_{M_2-\text{amp}}$ and $E^{\text{grid}-\text{R5}}_{M_2-\text{phase}}$ are presented in Table 2 for all grids considered for the entire domain (i.e., at all 147 elevation stations discussed in Section 3) as well as for various groups of stations defined in the previous section.

4.1. *Resolution requirements for tidal computations*

In the first numerical experiment, we examined the sensitivity of the solution to the level of refinement using a regular grid structure by comparing simulations for grids R1 through R5. Grid R1, shown in Fig. 3, is very coarsely discretized with a resolution of approximately $1.6° \times 1.6°$ (this corresponds roughly to 140 km × 140 km). The degree of resolution for both bathymetry and the coastal boundary is identical to that of the grid itself. The only islands included in grid R1 are Cuba and Hispaniola. Fig. 8 shows the M_2 wavelength to grid size ratio ($\lambda_{M_2}/\Delta x$) based on inviscid linear long wave theory and indicates that large portions of the continental shelf are significantly underresolved (regions where $\lambda_{M_2}/\Delta x \leqslant 12.5$). In fact, Table 1 indicates that the shallowest regions of the domain are quite poorly resolved with $\lambda_{M_2}/\Delta x$ as low as 1.5. Grid R2 is derived from grid R1 by splitting each element into four elements. This halves the resolution to approximately $0.8° \times 0.8°$ (roughly 70 km × 70 km). The coastal boundary remains identical to that of grid R1 although the bathymetric resolution was updated to be consistent with the resolution in the grid. This effectively steepens the gradient of the con-

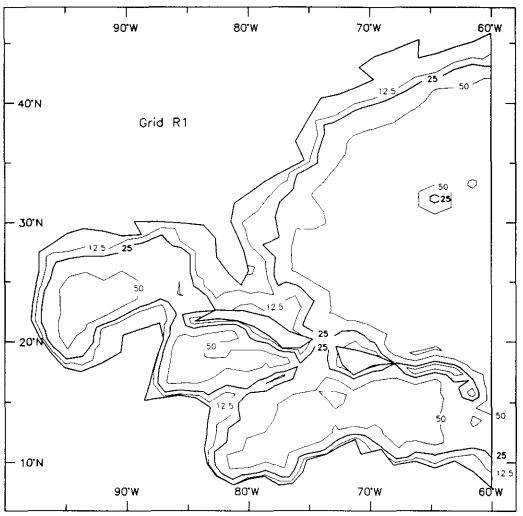

Fig. 8. Distribution of $\lambda_{M_2}/\Delta x$ contours for Grid R1.

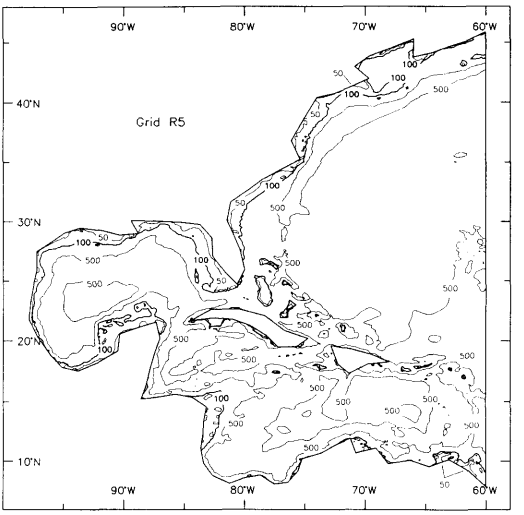

Fig. 9. Distribution of $\lambda_{M_2}/\Delta x$ contours for Grid R5.

tinental slope and improves the representation of the continental shelf. Grids R3 and R4 were subsequently generated in the same manner as grid R2, each increasing the grid resolution by a factor of 2 as compared to the previous grid while maintaining the same coastal boundary as grid R1 and updating the bathymetry to the resolution of the grid itself. Consequently grid R4 is finely discretized over the domain with a resolution of approximately $12' \times 12'$ (roughly 17 km × 17 km). Finally, grid R5 was generated by increasing the grid resolution by a factor of 2 in regions with bathymetry less than 3500 m while maintaining the same resolution as grid R4 in waters deeper than 3500 m. The resulting grid is shown in Fig. 4. Fig. 9 plots the $\lambda_{M_2}/\Delta x$ ratio for grid R5. The minimum $\lambda_{M_2}/\Delta x$ ratio is equal to approximately 23 which should be sufficient to resolve M_2 waves accurately in regions where topography does not vary rapidly. This assertion is based on the results of Fourier analysis briefly discussed in the section on the governing equations and the numerical discretization. We also note from Fig. 9 that all regions in grid R5 with rapidly varying topography, i.e., the continental shelf break and slope, as well as the deep ocean are resolved with $\lambda_{M_2}/\Delta x$ ratios ranging from approximately 100 to over 500.

The computed M_2 response at the 147 established elevation stations indicated that amplitudes typically tend to increase when comparing grids R1 and R2 and may increase or decrease when comparing grids R2 and R3, grids R3 and R4 and grids R4 and R5. There are a variety of factors which come into play when considering the convergences of these solutions. First, as the grid resolution improves, the M_2 wave is better resolved in the shallowest portions of the domain, at least on a local basis, and in regions of rapidly varying flow such as in the vicinity of the continental shelf break and slope. This improved resolution leads to reduced truncation errors in these regions. Second, as grid resolution increases, the continental shelf and slope are more accurately represented. Therefore, the interaction between the tides and topography as well as the importance of the bottom friction term will be altered.

Error measures for M_2 amplitude and phase are presented in Table 2. In general, the differences between solutions for subsequent grids become increasingly smaller with the finer grids. Errors tend to be largest in the Gulf of Mexico and Caribbean Sea and smallest in deep water. The relatively large amplitude and phase errors in the Gulf of Mexico are predominantly caused by large errors at a few stations along the coast of northern Florida and the Mississippi delta (stations 24, 25, 26, 27, 28, 96 and 98) in addition to stations near the center of the Gulf (stations 37, 82, 102). The absolute phase differences between grids R4 and R5 associated with these stations range between

Table 2a. *M_2 elevation amplitude errors, $E^{grid-R5}_{M_2-amp}$, for the grids applied in the convergence study as compared to the converged solution obtained with grid R5 for various regions within the domain*

	$E^{grid-R5}_{M_2-amp}$								
		Stations with measurement data				Additional stations without measurement data			
Grid	entire domain stations 1–147	US East Coast stations 1–20	Gulf of Mexico stations 21–38	Caribbean Sea stations 39–58	remote stations 59–77	Continental shelf stations 78–109	vicinity of the shelf break stations 88–109	vicinity of the toe of the slope stations 110–130	deep ocean stations 131–147
R1	0.293	0.303	0.593	0.524	0.083	0.339	0.121	0.112	0.091
R2	0.113	0.107	0.423	0.202	0.022	0.102	0.065	0.113	0.089
R3	0.033	0.025	0.139	0.089	0.010	0.032	0.031	0.050	0.039
R4	0.013	0.013	0.026	0.025	0.005	0.008	0.011	0.015	0.012
V1	0.022	0.022	0.037	0.042	0.008	0.025	0.013	0.015	0.012
V2	0.024	0.024	0.043	0.049	0.011	0.013	0.023	0.033	0.026
V3	0.160	0.170	0.154	0.264	0.032	0.176	0.079	0.111	0.087

Table 2b. *M_2 elevation phase errors, $E^{grid-R5}_{M_2-phase}$, for the grids applied in the convergence study as compared to the converged solution obtained with grid R5 for various regions within the domain*

	$E^{grid-R5}_{M_2-phase}$ (°)								
		Stations with measurement data				Additional stations without measurement data			
Grid	entire domain stations 1–147	US East Coast stations 1–20	Gulf of Mexico stations 21–38	Caribbean Sea stations 39–58	remote stations 59–77	Continental shelf stations 78–109	vicinity of the shelf break stations 88–109	vicinity of the toe of the slope stations 110–130	deep ocean stations 131–147
R1	20.9	31.6	30.1	29.1	8.4	22.4	19.4	15.1	12.0
R2	9.9	11.9	12.9	21.1	2.3	7.2	10.5	6.3	5.3
R3	3.4	4.5	6.8	5.6	0.95	2.5	3.1	1.9	1.7
R4	2.3	1.5	6.3	3.2	0.31	1.9	2.3	2.0	1.2
V1	3.2	1.6	10.4	2.6	0.33	3.0	3.6	2.8	1.3
V2	3.1	3.5	9.6	1.8	0.53	3.3	2.9	2.5	1.4
V3	14.6	16.1	41.5	14.2	2.2	12.2	13.6	10.9	6.2

8.8° and 17.6°. These stations lie in the vicinity of very high gradients in phase which occur on the Florida shelf, off the Mississippi delta and near the center of the Gulf associated with amphidromes. The increased error levels within the Caribbean are associated with stations in the vicinity of Puerto Rico and Hispaniola (stations 50 and 54) which are again located in the vicinity of high gradients in phase associated with an amphidrome. Based on the errors in Table 2, we judge that the resolution provided in grid R5 allows M_2 amplitudes to be predicted with less than 1% error and M_2 phase with less than 2 degrees error (based on the diminishing error trends since accuracy of grid R5 must be better than that of grid R4) expect at a few specific locations in the Gulf of Mexico and the Caribbean mentioned above. We consider the M_2 constituent solution obtained with grid R5 to be a converged solution for most of the WNAT domain with a coarse coastal boundary. Finally, we note that the errors in the computed overtides were not as good as for the astronomical M_2 tide. For

example, the M_6 constituent differed by an average of 21% in amplitude and 18° in phase between grids R4 and R5 within the domain. Thus grid R5 does not lead to converged overtide solutions.

4.2. *Development of an optimal graded mesh*

In the second experiment, unstructured graded grids were developed with the goal of obtaining M_2 solutions that were comparable to the finest regular mesh, grid R5. We note that while grid R5 adequately resolves the M_2 tide in the shallowest portions of the domain, it significantly over-resolves the M_2 tide in the deepest portions of the domain. In fact, Table 1 indicates that there are more than 1322 nodes per M_2 wavelength for the deepest waters. Over-resolving a grid to this extent is of course extremely inefficient from a computational perspective. Therefore we developed grids V1 and V2.

Grid V1, shown in Fig. 5, was generated by starting with grid R1 and systematically refining regions for which $\lambda_{M_2}/\Delta x \leqslant 25$ until the shallowest regions within the domain as well as the coastal boundary were discretized to approximately the same level of detail as grid R5. Thus grid V1 is coarsely resolved in deep water (1.6° resolution) and very finely resolved in the shallowest portions of the domain (5′ resolution). Regions with steep gradients in bathymetry such as in the vicinity of the continental shelf break and over the continental slope were generally refined to satisfy the minimum criterion $50 \leqslant \lambda_{M_2}/\Delta x \leqslant 100$. This criteria was based on one-dimensional numerical experiments and truncation error analysis which indicated that the $\lambda_{M_2}/\Delta x = 25$ is not adequate to give accurate solutions over the shelf break and slope (Westerink et al., 1992b). Transition regions between small and large elements were provided with additional resolution to create a smooth transition between element sizes and to control element skewness. We note that grid V1 maintains the same coarse coastal boundary as grids R1 through R5. Fig. 10 shows the distribution of $\lambda_{M_2}/\Delta x$ contours for grid V1 and indicates that the $\lambda_{M_2}/\Delta x$ ratio is generally between 25 and 50 on the continental shelf and ranges between 75 and 100 in deep waters. Over the continental shelf break and slope, $\lambda_{M_2}/\Delta x$ generally varies between 50 and 100 although in the Caribbean Sea, the ratio is as high as 250.

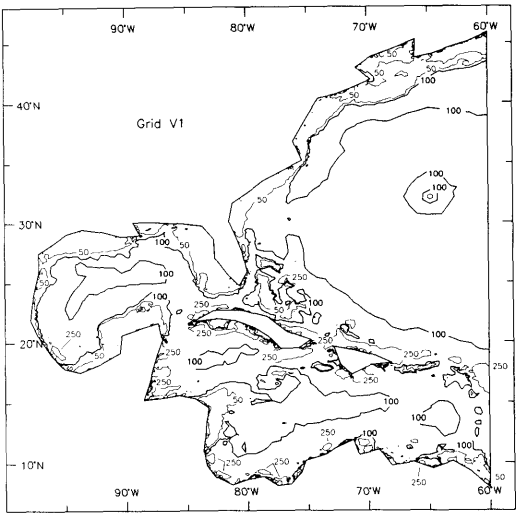

Fig. 10. Distribution of $\lambda_{M_2}/\Delta x$ contours for Grid V1.

The computed errors in Table 2 indicate that grid V1 gives almost the same response as grid R5. In fact, differences in M_2 amplitude between grids R5 and V1 are on the order of 2% and differences in phase are on the order of 3°. As was the case in the regular grid convergence studies, the Gulf of Mexico and Caribbean exhibit larger amplitude and phase errors than other portions of the domain. In particular, the Gulf of Mexico has large phase errors associated with stations along the coast of northern Florida and the Mississippi delta (stations 24 through 28 and 96), in the center of the Gulf (station 37), in addition to the southwestern portion of the Gulf (stations 82, 99, 102, 127). Again we note that these errors correspond to the large gradients in phase associated with amphidromes on the Florida shelf and in the center of the Gulf.

Finally, a second graded grid, Fig. 6, was developed to determine whether insufficient resolution over the shelf break, slope and selected deep regions were limiting factors in the agreement between grids R5 and V1. Grid V2, was developed, from grid V1 by providing resolution of at least 5′ in the vicinity of the continental shelf break (typically between 100 m and 500 m) and of at least 10′ on the slope (typically between 500 m and 4000 m). Again additional resolution was provided in adjacent regions in order to control the ratio of adjacent element sizes as well as element skewness.

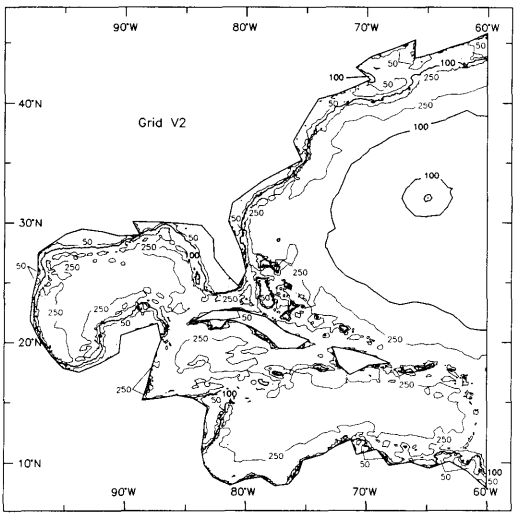

Fig. 11. Distribution of $\lambda_{M_2}/\Delta x$ contours for Grid V2.

Additional resolution was also provided in the deep regions of the Gulf and Caribbean. Grid V2 also maintains a coarse coastal boundary. Fig. 11 presents the $\lambda_{M_2}/\Delta x$ ratios for grid V2 and indicates that the $\lambda_{M_2}/\Delta x$ ratio in the vicinity of the continental shelf break, slope and in deep waters in the Gulf and Caribbean is much greater than for grid V1 (i.e., $\lambda_{M_2}/\Delta x$ is equal to at least 250 and often greater than 500) whereas other regions are similarly discretized.

Table 2 compares the M_2 amplitude response obtained with grids R5 and V2 at the 147 elevation stations. We note that the response of the graded grid V2 is almost identical to the response of the graded grid V1. Thus the resolution provided by grid V1 over the shelf break, slope and in deep waters in the Gulf and Caribbean does not limit the accuracy of the solution. In fact we can conclude that grid V2 unnecessarily over-resolves the shelf break and slope regions.

4.3. The influence of the resolution of the coastal boundary on the M_2 response

In the third experiment, we examined the sensitivity of the solution to the degree of resolution of the coastal boundary itself. Grids R1 through R5 as well as grids V1 and V2 all represented the coastal boundary with the resolution of the coarsest grid R1. Therefore we generated grid V3, shown in Fig. 7, from grid V1 by updating all coastal boundaries to a resolution of roughly 5′ (equivalent to the resolution of the most resolved regions in grid V1). The islands of Puerto Rico, Andros and Jamaica in addition to 50 smaller islands were also added. Table 2 indicates that the M_2 elevation response changes substantially in some regions with the improved representation of the coastal boundary. Particularly in near coastal regions and on the continental shelf, the resolution of the coastal boundary will strongly influence the computed response. Differences in phase in the Gulf of Mexico are particularly large. Differences in amplitude and phase are less in remote and deep waters.

5. Comparison between computed and observed tidal elevations in the WNAT model

We now present computations using the optimal graded grid V3 driven on the open ocean boundary using results from an existing global model and within the interior domain with 8 diurnal and semi-diurnal astronomical tidal constituents. These computations allow for realistic comparisons between the coupled global/WNAT model results and the measurement data at the 77 stations previously defined since the constituents are allowed to fully interact through the various nonlinear terms in the shallow water equations (Westerink et al., 1989). The computations were intended to be entirely predictive and therefore no calibration/tunning procedures were performed.

The open ocean boundary was forced using tidal elevations for the K_1, O_1, P_1, Q_1, M_2, S_2, N_2 and K_2 constituents from Schwiderski's global model (Schwiderski, 1979; 1981a–q). An effective tidal potential forcing within the interior domain was applied for the same 8 constituents that were forced on the open ocean boundary. Tidal potential amplitudes and the associated effective Earth elasticity factors for the 8 constituents are listed in Table 3. We note in particular that the diurnal tides have associated effective Earth elasticity factors ranging between 0.695 and 0.782 (Wahr, 1981; Woodworth, 1990) instead of the widely used value of 0.69 (Schwiderski, 1980; Hendershott, 1981). Equilibrium tides were directly computed and therefore no nodal factors or astronomical

Table 3. *Tidal potential constants for the principle tidal constituents (Reid, 1990) and the associated effective earth elasticity factor (Wahr, 1981)*

Species j	n	Constituent	T_{jn} (h)	C_{jn} (m)	α_{jn}
1	1	K_1 luni-solar	23.934470	0.141565	0.736
	2	O_1 principal lunar	25.819342	0.100514	0.695
	3	P_1 principal solar	24.065890	0.046843	0.706
	4	Q_1 elliptical lunar	26.868357	0.019256	0.695
2	1	M_2 principal lunar	12.420601	0.242334	0.693
	2	S_2 principal solar	12.000000	0.112841	0.693
	3	N_2 elliptical lunar	12.658348	0.046398	0.693
	4	K_2 luni-solar	11.967235	0.030704	0.693

arguments were used in either the boundary or the interior domain forcing functions.

A constant bottom friction coefficient equal to $C_f = 0.003$ was applied throughout the domain. Furthermore, all nonlinearities in the shallow water eqs., (1)–(3), were included in the computations. The model was spun up from homogeneous initial conditions using a 12-day hyperbolic tangent ramp function. Due to the presence of free Helmholtz modes within the Gulf of Mexico and Caribbean, results were only recorded after 40 days when these free modes had been entirely dissipated. The simulations were run for 225 days of which the last 185 days were recorded every half hour at elevation stations for which measurement data is available (stations 1–77) and every hour at all nodes within the domain. A time step of 37.5 s was used giving a Courant number between 0.01 and 1.1.

The computed time histories at all nodes within the domain as well as at the 77 measurement tidal elevation stations were harmonically analyzed over the recorded 185-day period. Cotidal charts for the 4 diurnal constituents and the 4 semi-diurnal constituents are presented in Figs. 12 and 13, respectively. These figures also indicate the relative error between the predicted and measured values at the 77 measurement stations for which data is available. Figs. 12, 13 indicate a marked similarity between each of the diurnal and each of the semi-diurnal constituents. The diurnal constituent amplitudes tend to increase significantly within the Gulf of Mexico. The diurnal constituents exhibit an amphidrome in the North Atlantic off the coast of Nova Scotia as well as dual amphidromes in the vicinity of the Bahamas. The semi-diurnal constituents experience rapid increases in amplitude in the Gulf of Maine, on the Blake Plateau, on the Florida Shelf, on the Nicaragua Rise as well as in the vicinity of Trinidad. Semi-diurnal amplitudes generally tend to be significantly smaller in the Gulf of Mexico and Caribbean than in the Atlantic. Full or degenerate amphidromes exists off of Puerto Rico and on the Florida Shelf. A full amphidrome exists in the center of the Gulf of Mexico for the M_2 and N_2 constituents while this feature appears as a degenerate amphidrome off of Cancun for the S_2 and K_2 constituents. A full amphidrome exists in the northwest Gulf of Mexico for the K_2 constituent.

The accuracy of the predicted tides was quantified by comparing predicted values at the 77 measurement stations for the 8 astronomical constituents to the available field data in harmonic form. The amplitude error for constituent j for each of the 8 astronomical constituents was computed as a proportional standard deviation for a defined region as:

$$E_{j-\text{amp}}^{\text{V3}-\text{meas}} \equiv \left[\frac{\sum_{l=1}^{L} [\hat{\eta}_j^{\text{V3}}(x_l, y_l) - \hat{\eta}_j^{\text{meas}}(x_l, y_l)]^2}{\sum_{l=1}^{L} [\hat{\eta}_j^{\text{meas}}(x_l, y_l)]^2} \right]^{1/2} \quad (13)$$

where

L = the total number of elevation stations within a given region,
(x_l, y_l) = the location of an elevation station,
$\hat{\eta}_j^{\text{V3}}(x_l, y_l)$ = the computed elevation amplitude for constituent j at station coordinates (x_l, y_l),
$\hat{\eta}_j^{\text{meas}}(x_l, y_l)$ = the measured elevation amplitude for constituent j at station coordinates (x_l, y_l).

The phase error for each constituent j was computed as an absolute average error defined over a region as:

$$E_{j-\text{phase}}^{\text{V3}-\text{meas}} \equiv \frac{1}{L} \sum_{l=1}^{L} |\phi_j^{\text{V3}}(x_l, y_l) - \phi_j^{\text{meas}}(x_l, y_l)|, \quad (14)$$

where

$\phi_j^{V3}(x_l, y_l)$ = the computed elevation phase for constituent j at measurement location (x_l, y_l),

$\phi_j^{meas}(x_l, y_l)$ = the measured elevation phase for constituent j at measurement location (x_l, y_l).

The amplitude and phase errors are presented in Table 4 for the entire domain as well as on a regional basis for each of the 8 astronomical constituents. The constituents are predicted with an average amplitude error of between 18.2% and 45.3% and an average phase error of between 8.3 and 27.5 degrees. Typically, the larger constituents, the K_1, O_1, M_2, S_2 and N_2 tides, have smaller relative amplitude errors while the smaller constituents, the P_1, Q_1 and K_2 tides, have larger relative amplitude errors. There are no predominant trends with respect to spatial variability in amplitude errors with the exception of relatively lower errors in the Caribbean for diurnal constituents and relatively higher errors in the Caribbean and Gulf of Mexico for semi-diurnal constituents. The distribution of amplitude ratio errors, presented in Table 5a, indicates that the diurnal constituent amplitude predictions are evenly and closely clustered about the measured values while the semi-diurnal constituent amplitude predictions are typically overpredicted with quite a few outliers. Phase errors for the diurnal tides, ranging between 8.6° and 12.4° error, are much smaller than phase errors for the semi-diurnal tides which range between 19.6° and 27.5°. Phase errors tend to be especially large for the semi-diurnal constituents within the Gulf of Mexico and Caribbean. A consistent feature of our results is that stations which had poor convergence properties also showed the poorest comparison to the measurement data. Again these stations typically lie in the vicinity of amphidromes. Finally, the relative distribution of phase errors is presented in Table 5b which indicates that predicted diurnal constituent phases generally lead and are clustered closely about the measured phase while predicted semi-diurnal constituent errors are distributed over a much wider range of values.

On a CRAY YMP-6128, ADCIRC-2DDI ran at 0.46 central processing unit seconds per time step for the WNAT domain using grid V3.

6. Discussion

The overall accuracy of a numerical model depends on the physics included in the model, on the numerical accuracy (which depends on the algorithm as well as the grid) and on the precision of the forcing functions. Two-dimensional barotropic tidal models generally give comparisons between model predictions and measurements within 10% accuracy for amplitude and 10° accuracy for phase. Therefore we can assume that the physics incorporated in our model should be generally satisfactory.

The WNAT model grid convergence studies demonstrate that we have generally converged to solutions within 1% to 2% error in amplitude and 2° to 3° in phase with the exception of the Gulf of Mexico and Caribbean where persistent errors occur in semi-diurnal constituents phases. The latter problem appears to be associated with amphidromes whose locations shift readily. The performance characteristics of our finest regular grid ($6' \times 6'$ to $12' \times 12'$ in very deep water) and our unstructured graded V1 and V2 grids were very similar. All three grids appear to have difficulties in phase in the Gulf of Mexico and Caribbean with an average error of up to 10°. The results from grids V1, V2 and R5 indicate that the lack of convergence in the Gulf as well as in the Caribbean is not associated with insufficient resolution over the shelf break, slope, in deep waters or in the immediate vicinity of the amphidromes. Rather these problems appear to be due to factors which control the structure and location of the amphidromes. Previous studies that we have done in the Gulf indicate that the semi-diurnal response was very sensitive to the grid resolution, bathymetry as well as the bottom friction coefficient (Westerink et al., 1992a). We believe that it is most likely that insufficient resolution over the shelf, particularly in the shallowest regions, may be responsible for the relatively poor numerical convergence in these regions. Finally grid V3 clearly demonstrated the importance of providing detailed resolution for the coastal boundary. Phase response in the Gulf was again the most sensitive.

The results of the uncalibrated simulation in which the optimal graded grid V3 is forced with Schwiderski's (1979, 1981a–q) global model indicate that the differences between the WNAT model predictions and field data significantly exceed the

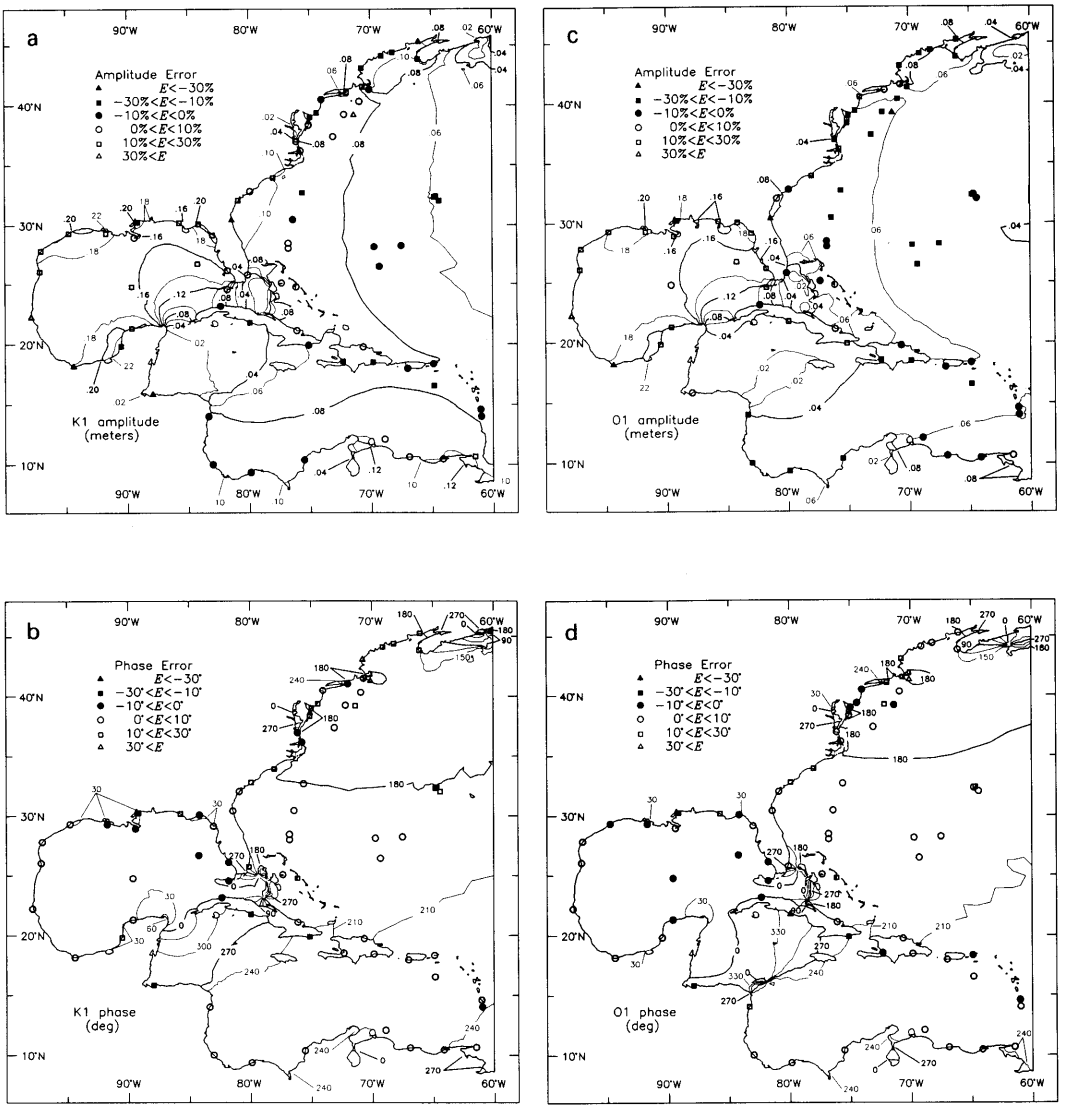

Fig. 12. Computed contours for elevation amplitudes (m) and phases (in ° relative to GMT) for the four diurnal astronomical tidal constituents used in the boundary and interior domain forcing functions.

level of estimated numerical convergence error throughout the entire domain. Nonetheless, the largest errors again occur in the Gulf of Mexico as well as the Caribbean. Many of the largest semi-diurnal constituent station errors occur in the vicinity of amphidromic points. This suggests that the amphidromes are sensitive not only to numerical truncation errors and the resolution provided for the coastal boundary but also to the precision of the forcing function. Indeed a systematic error for all constituents exists in amplitude and phase throughout the entire domain in deep as well as shallow waters. It is highly likely that Schwiderski's model is not sufficiently accurate on our WNAT model open ocean boundary. In fact, Cartwright and Ray (1991) computed root

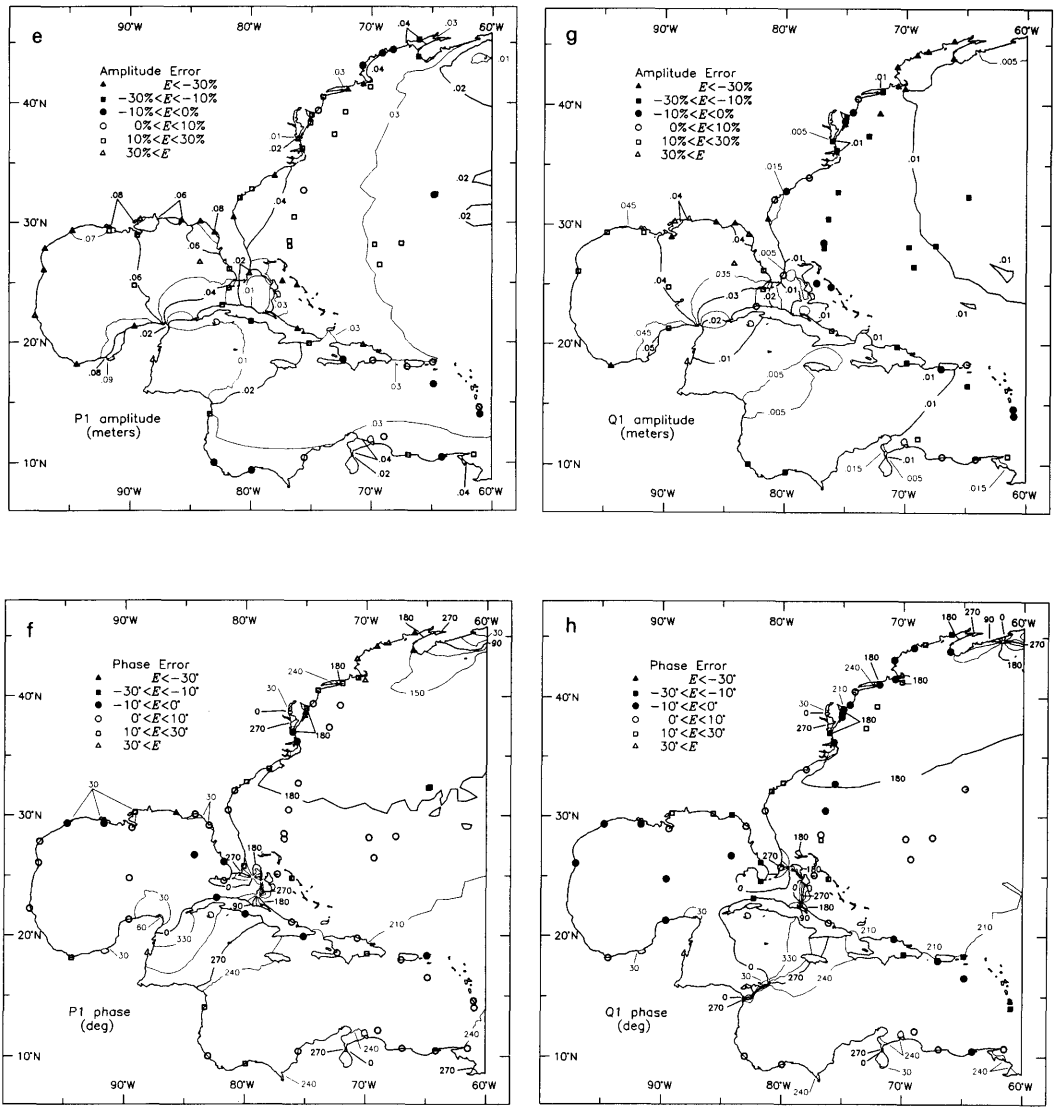

Fig. 12. Continued.

mean square errors at 80 deep ocean stations throughout the world and found average amplitude errors of 4.1 cm for M_2, 1.86 cm for S_2, 1.49 cm for O_1 and 1.76 cm for K_1. How these globally average errors exactly impact the constituent values used on the WNAT model open ocean boundary is difficult to determine. However since the tides are typically small in deep waters, errors in Schwiderski's results on this boundary may be significant. We are currently performing sensitivity studies for the forcing functions on the open ocean boundary to determine the exact degree of sensitivity and will report on these findings in a later paper.

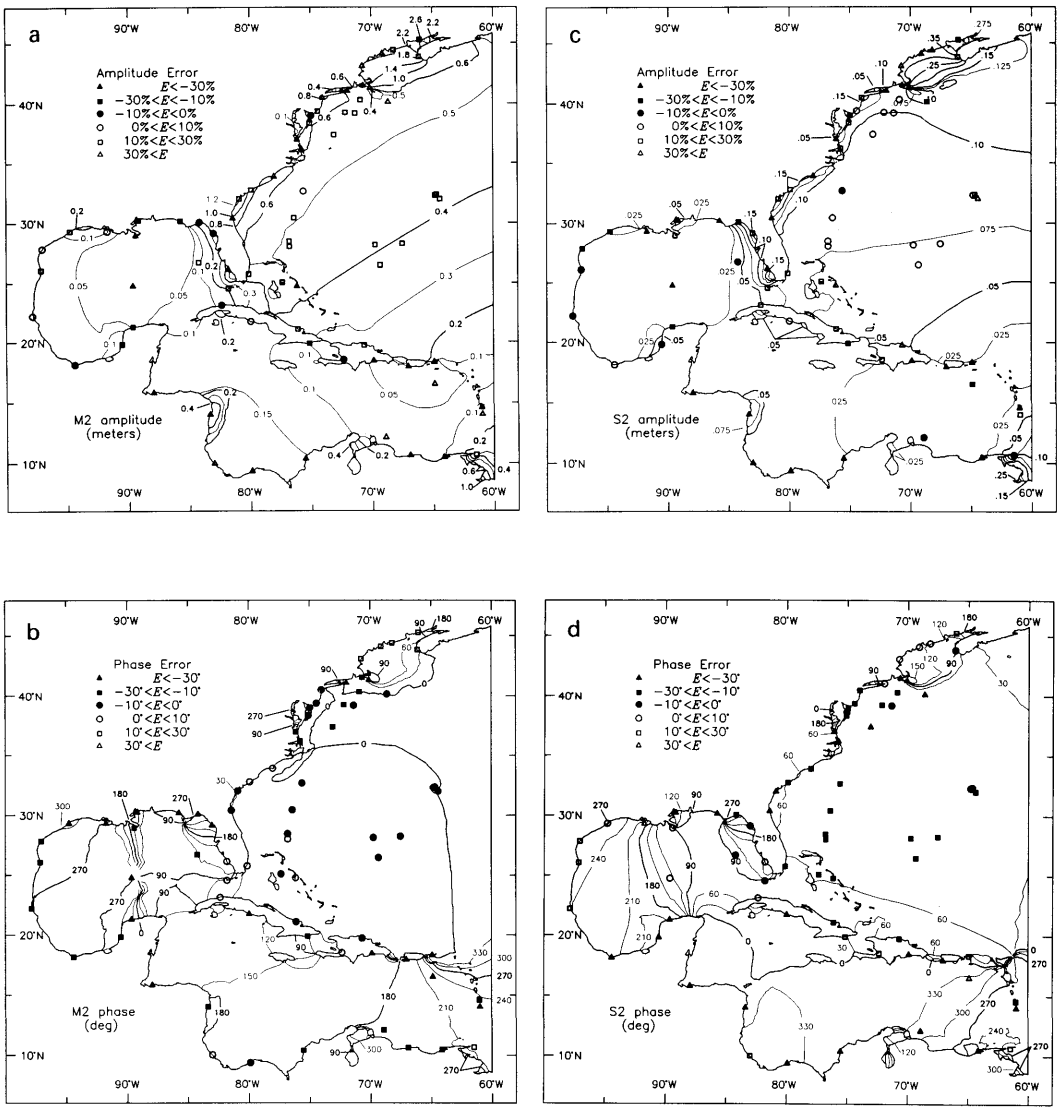

Fig. 13. Computed contours for elevation amplitudes (m) and phases (in ° relative to GMT) for the four semi-diurnal astronomical tidal constituents used in the boundary and interior domain forcing functions.

7. Conclusions

The WNAT model is a large domain coastal model with a geometrically and hydrodynamically simple ocean boundary which is ideally located to facilitate tidal predictions with minimum requirements for open ocean boundary condition calibration. The open ocean boundary lies almost entirely in deep water where astronomical tides vary slowly, nonlinear tides are small and global models, to which the WNAT model can be coupled, are likely to be most accurate. Due to the resulting large domain and the required resolution in shallow regions as well as regions of rapidly varying flow, it is highly desirable to vary nodal densities to fully resolve flow features on a local

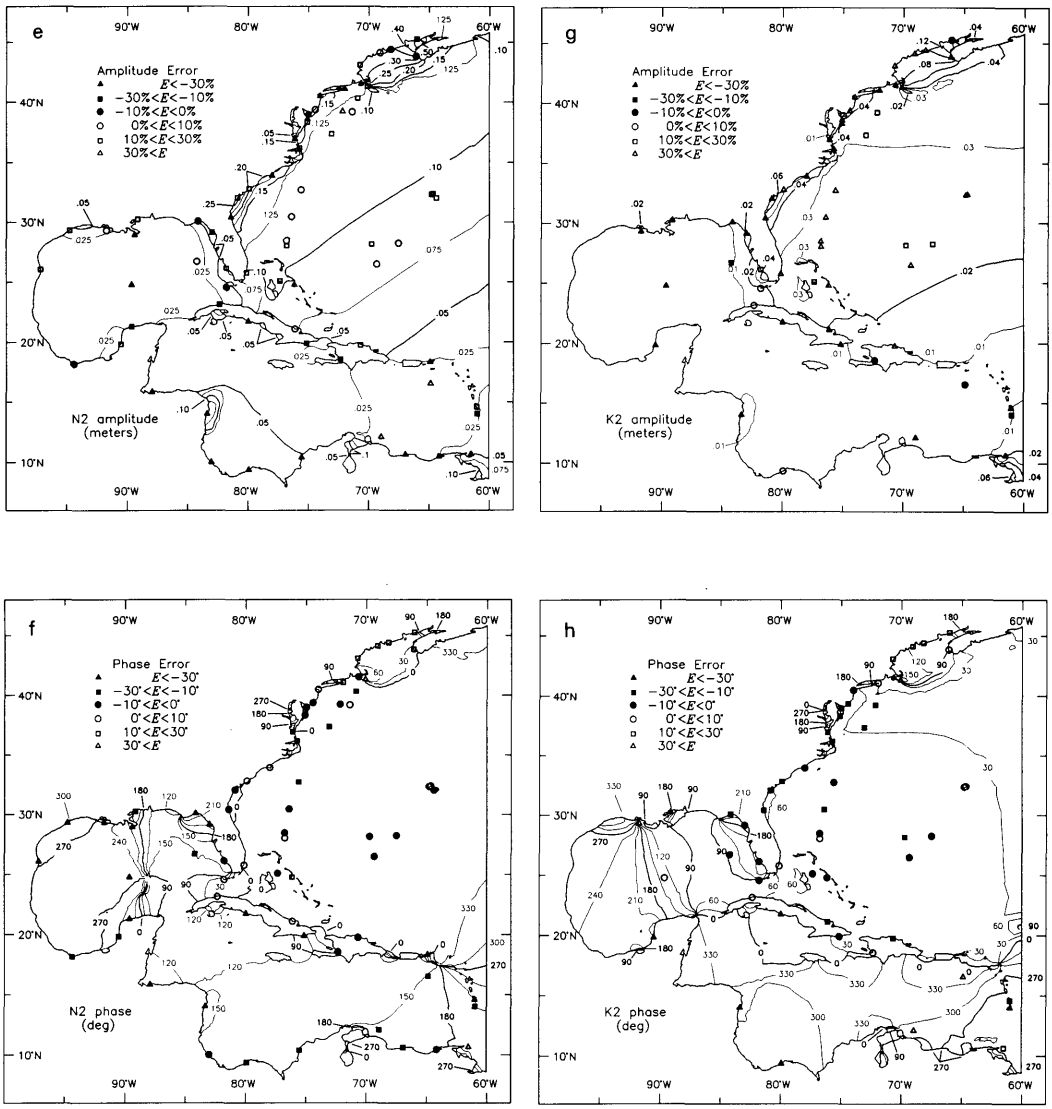

Fig. 13. Continued.

basis. The FE shallow water equation model, ADCIRC-2DDI, easily accomodates the required highly flexible meshes.

We have systematically studied resolution requirements using the entire WNAT model domain and a sequence of regular grids (with grids ranging from a very coarse $1.6° \times 1.6°$ mesh to a very fine $6' \times 6'$ to $12' \times 12'$ mesh) as well as a sequence of unstructured graded grids with resolution varying between 1.6° and 5′ within each mesh. Elevation response computations with the sequence of regular grids indicate that the semidiurnal M_2 tide typically converges to better than 1% accuracy in elevation amplitude and 2 degrees in phase using the $6' \times 6'$ to $12' \times 12'$ mesh with the exception of specific locations in the Gulf of Mexico and Caribbean in which shifting amphidromes lead to consistently larger phase

Table 4a. *Amplitude errors, $E_{j-amp}^{V3-meas}$, for constituent j computed using grid V3 as compared to field measured values for various regions within the domain*

		$E_{j-amp}^{V3-meas}$				
j	Constituent	entire domain stations 1–77	US East Coast stations 1–20	Gulf of Mexico stations 21–38	Caribbean Sea stations 39–58	remote stations 59–77
1	K_1	0.182	0.220	0.199	0.077	0.131
2	O_1	0.205	0.212	0.218	0.109	0.199
3	P_1	0.345	0.289	0.453	0.167	0.235
4	Q_1	0.324	0.336	0.356	0.131	0.251
5	M_2	0.270	0.266	0.278	0.652	0.204
6	S_2	0.290	0.288	0.407	0.529	0.122
7	N_2	0.244	0.234	0.124	0.741	0.154
8	K_2	0.453	0.444	0.546	0.455	0.407

Table 4b. *Phase errors, $E_{j-phase}^{V3-meas}$, for constituent j computed using grid V3 as compared to field measured values for various regions within the domain*

		$E_{j-phase}^{V3-meas}$				
j	Constituent	entire domain stations 1–77	US East Coast stations 1–20	Gulf of Mexico stations 21–38	Caribbean Sea stations 39–58	remote stations 59–77
1	K_1	9.5	17.6	7.8	5.6	6.7
2	O_1	8.3	9.5	7.2	9.9	6.3
3	P_1	12.4	23.4	7.5	7.1	9.4
4	Q_1	8.6	8.0	9.6	9.4	7.5
5	M_2	22.4	15.1	33.1	31.2	10.8
6	S_2	27.5	20.2	28.7	40.8	20.6
7	N_2	19.6	13.6	37.4	23.9	8.0
8	K_2	23.6	15.0	44.5	35.8	12.7

Table 5a. *Distribution of amplitude ratio error, $R_a = \hat{\eta}_j^{V3}(x_l, y_l)/\hat{\eta}_j^{meas}(x_l, y_l)$, for the measurement stations*

		% distribution of R_a												
j	Constituent	$R_a < 0.5$	$0.5 \leqslant R_a < 0.6$	$0.6 < R_a \leqslant 0.7$	$0.7 < R_a \leqslant 0.8$	$0.8 < R_a \leqslant 0.9$	$0.9 < R_a \leqslant 1.0$	$1.0 < R_a \leqslant 1.1$	$1.1 < R_a \leqslant 1.2$	$1.2 < R_a \leqslant 1.3$	$1.3 < R_a \leqslant 1.4$	$1.4 < R_a \leqslant 1.5$	$1.5 < R_a \leqslant 2.0$	$2.0 < R_a$
1	K_1	0.0	0.0	2.6	7.9	11.8	21.1	26.3	11.8	10.5	6.6	1.3	0.0	0.0
2	O_1	0.0	0.0	1.3	11.8	22.4	21.1	10.5	18.4	9.2	5.3	0.0	0.0	0.0
3	P_1	0.0	0.0	0.0	1.4	4.3	14.3	11.4	10.0	25.7	10.0	5.7	17.1	0.0
4	Q_1	0.0	6.4	8.1	9.7	17.7	14.5	12.9	9.7	6.5	3.2	4.8	6.5	0.0
5	M_2	1.3	2.6	0.0	3.9	2.6	7.8	6.5	23.4	15.6	11.7	3.9	9.1	13.7
6	S_2	2.6	1.3	0.0	2.6	9.2	10.5	18.4	13.1	7.9	11.8	2.6	9.2	10.5
7	N_2	1.4	2.9	1.4	5.7	5.7	7.1	17.1	20.0	11.4	10.0	4.3	7.1	5.7
8	K_2	7.2	7.1	3.6	0.0	5.4	5.4	7.1	3.6	7.1	10.7	7.1	28.6	7.1

Table 5b. *Distribution of phase error, $P_d = \phi_j^{V3}(x_l, y_l) - \phi_j^{meas}(x_l, y_l)$, for the measurement stations*

		% distribution of R_a											
j	Constituent	$-180 < P_d \leqslant -60$	$-60 < P_d \leqslant -40$	$-40 < P_d \leqslant -30$	$-30 < P_d \leqslant -20$	$-20 < P_d \leqslant -10$	$-10 < P_d \leqslant 0$	$0 < P_d \leqslant 10$	$10 < P_d \leqslant 20$	$20 < P_d \leqslant 30$	$30 < P_d \leqslant 40$	$40 < P_d \leqslant 60$	$60 < P_d \leqslant 180$
1	K_1	0.0	0.0	0.0	0.0	3.9	15.8	51.3	13.2	10.5	1.3	3.9	0.0
2	O_1	0.0	0.0	1.3	2.6	0.0	22.4	55.3	13.2	2.6	1.3	1.3	0.0
3	P_1	0.0	0.0	0.0	0.0	0.0	15.7	50.0	12.9	8.6	10.0	2.9	0.0
4	Q_1	0.0	0.0	1.6	1.6	12.9	37.1	30.6	14.5	1.6	0.0	0.0	0.0
5	M_2	2.6	7.8	3.9	13.0	14.3	26.0	15.6	2.6	5.2	2.6	2.6	3.9
6	S_2	2.6	1.3	9.2	15.8	14.5	11.8	11.8	7.9	3.9	9.2	5.3	6.6
7	N_2	1.4	14.3	4.3	14.3	8.6	27.1	15.7	8.6	2.9	0.0	2.9	0.0
8	K_2	1.8	1.8	1.8	7.1	21.4	25.0	17.9	5.4	3.6	3.6	3.6	7.1

errors. The overtide constituents did not satisfactorily converge, even with the finest $6' \times 6'$ to $12' \times 12'$ mesh. The elevation response computed using the unstructured graded meshes achieve about the same level of performance as the finest nearly uniform grid. Overall these studies indicate that grids can be developed based on a $\lambda/\Delta x \simeq 25$ criterion with some additional resolution over the shelf break and slope. This is in sharp contrast with one dimensional studies which indicated the need for a much higher level of resolution over the continental shelf break and slope (Westerink et al., 1992b). This indicates the importance of performing grid convergence studies in two dimensions as opposed to one-dimension. However it appears that the shallow regions in the Gulf of Mexico and Caribbean need to be more highly resolved in order to converge to the same level of precision as in other parts of the domain. Finally, we noted that the representation of the coastal boundary can also substantially influence tidal response.

We performed predictive computations using our optimal graded mesh driven by the 8 constituents from Schwiderski's global ocean model results and by tidal potential functions. Comparisons of measurement data at 77 stations for the K_1, O_1, P_1, Q_1, M_2, S_2, N_2 and K_2 constituents indicate that these constituents are predicted with average errors in amplitude between 18.2% and 45.3% and average errors in phase of between 8.3° and 27.5°. Phase errors in the Gulf of Mexico and Caribbean for semi-diurnal constituents are quite sensitive to the shifting amphidromes. Even in deep water we fail to get a close match between predictions and measurements. We believe that Schwiderski's model results contribute substantially to these error levels. Currently we are looking at the sensitivity of the response to perturbations in the boundary forcing function in addition to driving our model boundary with more accurate global models.

8. Acknowledgments

This research was funded under contract DACW-39-90-K-0021 with the U.S. Army Engineers Waterways Experiment Station. We wish to thank Dr. Mike Foreman of the Institute of Ocean Sciences (IOS), Sidney, BC Canada for very helpful discussions. We also thank Dr. A. M. Baptista of the Oregon Graduate Institute for allowing us to use the software package Gredit and Dr. R. F. Henry of IOS and Dr. R. Walters of the USGS in Tacoma, WA for allowing us to use the software package TRIGRID.

REFERENCES

Cartwright, D. E. and Ray, R. D. 1991. Energetics of global ocean tides from geosat altimetry. *J. Geophys. Res.* **96**, C9, 16897–16912.

Dietrich, D. E., Roache, P. J. and Marietta, M. G. 1990. Convergence studies with the Sandia ocean modeling system. *International J. for Numerical Methods in Fluids* **11**, 127–150.

Flather, R. A. 1987. Estimates of extreme conditions of

tide and surge using a numerical model of the northwest European continental shelf. *Estuarine, Coastal and Shelf Science* **24**, 69–73.

Flather, R. A. 1988. A numerical model investigation of tides and diurnal-period continental shelf waves along Vancouver Island. *J. Physical Oceanography* **18**, 115–139.

Foreman, M. G. G. 1983. An analysis of the wave equation model for finite-element tidal computations *J. Computational Physics* **52**, 290–312.

Foreman, M. G. G. 1988. A comparison of tidal models for the southwest coast of Vancouver Island. In: *Proceedings of the VII International Conference on Computational methods in water resources*, held in Cambridge, MA. Elsevier.

Gerritsen, H. and Bijlsma, A. C. 1988. Modelling of tidal and wind-driven flow: the Dutch continental shelf model. In: *Computer modelling in ocean engineering* (eds. Schrefler and Zienkiewicz). Balkema, Rotterdam.

Gray, W. G. 1982. Some inadequacies of finite element models as simulators of two-dimensional circulation. *Advances in Water Resources* **5**, 171–177.

Gray, W. G. 1989. A finite element study of tidal flow data for the North Sea and English channel. *Advances in Water Resources* **12**, 143–154.

Hendershott, M. C. 1981. Long waves and ocean tides. In: *Evolution of physical oceanography*, pp. 292–341 (eds. B. A. Warren and C. Wunsch). MIT Press, Cambridge, MA.

International hydrographic organization tidal constituent bank 1991. Station Catalogue. Ocean and Aquatic Sciences, Department of Fisheries and Oceans, Ottawa.

Kinnmark, I. P. E. 1984. *The shallow water wave equations: formulation, analysis and application.* Ph.D. Dissertation, Department of Civil Engineering, Princeton University.

Kolar, R. L., Gray, W. G., Westerink, J. J. and Luettich, R. A. 1993. Shallow water modeling in spherical coordinates: equation formulation, numerical implementation, and application. *J. Hydraulic Research*, in press.

Le Provost, C. and Vincent, P. 1986. Some tests of precision for a finite element model of ocean tides. *J. Computational Physics* **65**, 273–291.

Luettich, R. A., Westerink, J. J. and Scheffner, N. W. 1992. ADCIRC: An advanced three-dimensional circulation model for shelves, coasts and estuaries, Report 1: Theory and methodology of ADCIRC-2DDI and ADCIRC-3DL. Dredging Research Program, *Technical Report DRP-92-6*, Department of the Army, Washington, DC.

Lynch, D. R. 1983. Progress in hydrodynamic modeling, review of US Contributions, 1979–1982. *Reviews of Geophysics and Space Physics* **21**, 741–754.

Lynch, D. R. and Gray, W. G. 1979. A wave equation model for finite element tidal computations. *Computers and Fluids* **7**, 207–228.

Pearson, F. 1990. *Map projections: theory and applications.* CRC Press, Boca Raton, Florida.

Platzman, G. W. 1981. Some response characteristics of finite element tidal models. *J. Computational Physics* **40**, 36–63.

Reid, R. O. and Whitaker, R. E. 1981. *Numerical model for astronomical tides in the gulf of Mexico.* Technical Report for the US Army Engineers, Department of Oceanography. Texas A & M University.

Reid, R. O. 1990. Waterlevel changes, tides and storm surges. In: *Handbook of coastal and ocean engineering* (ed. J. Herbich). Gulf Publishing, Houston, Texas.

Schwiderski, E. W. 1979. *Global ocean tides*, Part II: The semidiurnal principle lunar tide (M_2), atlas of tidal charts and maps. NSWC TR 79-414.

Schwiderski, E. W. 1980. On charting global ocean tides. *Reviews in Geophysics and Space Physics* **18**, 243–268.

Schwiderski, E. W. 1981a. *Global ocean tides*, Part III: The semidiurnal principle solar tide (S_2), atlas of tidal charts and maps. NSWC TR 81-122.

Schwiderski, E. W. 1981b. *Global ocean tides*, Part IV: The diurnal luni-solar declination tide (K_1), atlas of tidal charts and maps. NSWC TR 81-142.

Schwiderski, E. W. 1981c. *Global ocean tides*, Part V: The diurnal principle lunar tide (O_1), atlas of tidal charts and maps. NSWC TR 81–144.

Schwiderski, E. W. 1981d. *Global ocean tides*, Part VI: The semidiurnal elliptical lunar tide (N_2), atlas of tidal charts and maps. NSWC TR 81–218.

Schwiderski, E. W. 1981e. *Global ocean tides*, Part VII: The diurnal principle solar tide (P_1), atlas of tidal charts and maps. NSWC TR 81–220.

Schwiderski, E. W. 1981f. *Global ocean tides*, Part VIII: The semidiurnal luni-solar declination tide (K_2), atlas of tidal charts and maps. NSWC TR 81–222.

Schwiderski, E. W. 1981g. *Global ocean tides*, Part IX: The diurnal elliptical lunar tide (Q_1), atlas of tidal charts and maps. NSWC TR 81–224.

Turner, P. J. and Baptista, A. M. 1991. ACE/Gredit users manual: Software for semi-automatic generation of two-dimensional finite element grids. *CCALMR Software Report SDS2* (91-2), Oregon Graduate Institute, Beaverton, OR.

U.S. Geological Survey. 1984. Atlas of tidal elevation and current observations on the North-east American continental shelf and slope. US *Geological Survey Bulletin # 1611.*

Vincent, P. and Le Provost, C. 1988. Semidiurnal tides in the northeast Altantic from a finite element numerical model. *J. Geophys. Res.* **93**, C1, 543–555.

Wahr, J. M. 1981. Body tides on an elliptical, rotating, elastic and oceanless earth. *Geophysical J. Royal Astronomical Society* **64**, 677–703.

Walters, R. A. 1988. A finite element model for tides and currents with field applications. *Communications Applied Numerical Methods* **4**, 401–411.

Walters, R. A. and Werner, F. E. 1989. A comparison of two finite element models of tidal hydrodynamics using a North Sea data set. *Advances in Water Resources* **12**, 184–193.

Werner, F. E. and Lynch, D. R. 1989. Harmonic

structure of English channel/southern bight tides from a wave equation simulation. *Advances in Water Resources* **12**, 121–142.

Westerink, J. J., Stolzenbach, K. D. and Connor, J. J. 1989. General spectral computations of the nonlinear shallow water tidal interactions within the bight of Abaco. *J. of Physical Oceanography* **19**, 1348–1371.

Westerink, J. J. and Gray, W. G. 1991. Progress in surface water modeling. *Reviews of Geophysics* **29**, April suppl., 210–217.

Westerink, J. J., Luettich, R. A., Baptista, A. M., Scheffner, N. W. and Farrar, P. 1992a. Tide and storm surge predictions using a finite element model. *J. of Hydraulic Engineering* **118**, 1373–1390.

Westerink, J. J., Muccino, J. C. and Luettich, R. A. 1992b. Resolution requirements for a tidal model of the western North Atlantic and gulf of Mexico. In: *Proceedings of the IX International Conference on Computational methods in water resources*, Denver, CO, (eds. T. F. Russell et al.). Computational Mechanics Publications, Southampton, UK.

Woodworth, P. L. 1990. Summary of recommendations to the UK Earth Observation Data Centre (UK-EODC) by the Proudman Oceanographic Laboratory (POL) for tide model corrections on ERS-1 Geophysical Data Records. Proudman Oceanographic Laboratory Communication.